Article:

Gualandi, A, Liu, Z and Rollins, C (2020) Post-large earthquake seismic activities mediated by aseismic deformation processes. Earth and Planetary Science Letters, 530. 115870. ISSN 0012-821X

https://doi.org/10.1016/j.epsl.2019.115870

Post-large earthquake seismic activities mediated by aseismic deformation processes

Authors: A. Gualandi,[1] Z. Liu,[1] C. Rollins[2]

[1] National Aeronautics and Space Administration, Jet Propulsion Laboratory, California Institute of Technology, Pasadena, California, USA

[2] Department of Earth and Environmental Sciences, Michigan State University

Abstract

Two aseismic deformation processes are commonly invoked to explain the transient geodetic surface displacements that follow a major earthquake: afterslip and viscoelastic relaxation. Both induce time dependent stress variations in the crust, potentially affecting aftershock occurrence. However, the two mechanisms' relative impacts on crustal deformation and seismicity remain unclear. We find for the case of the 2010 M_w 7.2 El Mayor-Cucapah (EMC) earthquake not only that afterslip likely drove clustered seismicity after the earthquake, but also that long-range earthquake interactions were likely modulated by viscoelastic relaxation at large scales in space (>5 times the fault rupture length) and time (>7 years). This has important implications for the study of the "seismic cycle" and for seismic hazard estimation, since post-seismic deformation related to a single M_w 7.2 earthquake affects interseismic velocities and regional seismicity rates for more than a decade.

Introduction

After an earthquake, accelerated deformation processes in the crust and upper mantle accommodate the sudden coseismic stress changes. These include aftershocks and aseismic processes like afterslip (post-seismic slip on/around the co-seismic rupture), viscoelastic relaxation (lower crust/upper mantle stress-driven bulk flow), and poroelastic effects (pore pressure readjustments in the crust). The latter typically affect regions in the near-field of the coseismic rupture [e.g., Jónsson et al., 2003]. The terms interpreted as aseismic fault slip processes release an equivalent seismic moment typically ~10-40% that of the mainshock [Avouac, 2015], sometimes exceeding it [Freed, 2007; Bruhat et al., 2011]. They thus play a significant role in the moment budget of the “seismic cycle” [Bürgmann et al., 2008]. Aftershocks, which can be thought of as seismic afterslip, usually explain a smaller fraction of moment release than their aseismic counterpart on the fault [e.g., Perfettini and Avouac, 2007]. Although viscoelastic relaxation is usually the dominant mechanism of deformation in the long run [e.g., Suito and Freymueller, 2009], these mechanisms’ relative contributions are frequently debated because of trade-offs between them [Feigl and Thatcher, 2006; Bürgmann et al., 2008; Sun et al., 2014]. The links between these processes and aftershocks can shed light on the connections between seismic and aseismic deformation processes, and are a matter of ongoing research. In summary, two open questions are 1) Can we separate the multiple processes that may be active in the post-seismic stage? 2) If yes, is there any connection between the aseismic and seismic processes?

Post-seismic deformation following the 2010 M_w 7.2 El Mayor-Cucapah earthquake (EMC) (Figure 1), still persisting more than 7 years after the mainshock, provides an opportunity to address these questions. Although the geodetic and seismologic coverage is spatially asymmetric, it includes hundreds of GPS stations (Figure 1) and seismic catalogs with tens of thousands of events [Hauksson et al., 2012; Yang et al., 2012]. To analyze the GPS data, we apply a variational Bayesian Independent Component Analysis (vbICA) algorithm [Choudrey and Roberts, 2003] recently adapted to study GPS position time series with missing data [Gualandi et al., 2016]. This algorithm separates mixed signals into a finite set of sources of different physical origins by enforcing statistical independence between the sources’ temporal functions, without imposing a specific form to them (see Methods: Geodetic signal extraction). Its application to GPS position time series has already proven effective in separating deformation due to various tectonic and non-tectonic processes [Gualandi et al., 2017b; Serpelloni et al., 2018; Larochelle et al., 2018; Michel et al., 2018].

The analysis of aftershocks may be biased by the common assumption that they are superimposed on a background Poissonian process [Reasenberg, 1985], which has for example been proven wrong in Southern California [Luen and Stark, 2012]. We use a recently developed clustering algorithm [Zaliapin and Ben-Zion, 2013] that instead only considers the separation between pairs of two events in space and time and the magnitude of the first event in the pair. Thanks to these parallel approaches we isolate in each dataset (geodetic and seismic) a short- and long-term decay process. The aftershocks with small distances from EMC and the Mw 5.7 Ocotillo earthquake are clustered in space and show a rapid temporal decay, matching the short duration and near-field nature of inferred afterslip. The aftershocks with large distances from the mainshock (up to 800 km) are more distributed in space and their cumulative number evolves similarly to the inferred viscoelastic deformation process.

Geodetic and seismic data

We use the position time series generated by the Jet Propulsion Laboratory (ftp://sopac-ftp.ucsd.edu/pub/timeseries/measures/ats/WesternNorthAmerica/). In particular, we use the cleaned and detrended product up to 16 December 2017, consisting of daily sampled data. These time series have been corrected for a long-term linear trend and for eventual offsets (both instrumental and tectonic). The linear trend is estimated using all data available, and fitting the time series with a model consisting of secular rates, coseismic offsets, seasonal terms (annual and semiannual), postseismic parameters, nontectonic offsets primarily due to instrument or antenna changes, and other transient motion (for details, see Liu et al., 2010; Bock et al., 2016). Since some residual offsets are not well corrected at the time of the major seismic events, we correct them via a Principal Component Analysis, centering the analysis around the offset and then correcting for the retrieved step. We consider all the available epochs after the day of the EMC mainshock. We discard stations having more than 50% of missing data in the considered time span, as well as station BOMG because of clear local effects. After this selection, we end up with 125 GPS stations (Figure 1 and Table S1).

We use the Hauksson et al. (2012) and Yang et al. (2012) seismic catalogs updated to 30/06/2016 and 30/09/2016, respectively. They are available at: http://scedc.caltech.edu/research-tools/alt-2011-dd-hauksson-yang-shearer.html and http://scedc.caltech.edu/research-tools/alt-2011-yang-hauksson-shearer.html. We adopt a completeness magnitude of $M_c = 2.0$. The results obtained using the catalog by Hauksson et al. (2012) are reported in the Supplementary Material, while in the main text we show those from Yang et al. (2012).

Methods

Geodetic signal extraction

We adopt a multivariate statistic approach to study the GPS position time series. We organize the data in a matrix X such that each row is a different position time series and each column is a different epoch. The size of the matrix X is M×T, with M = 3×125 since we use all three GPS directions (east, north, and vertical) for each station, and T = 2784, corresponding to more than 7.5 years since we use daily data. We then center the data, i.e. we set the 0 for every time series to its average value. The various time series are considered as observed random variables and obtained as the realization of a mix of a reduced number of sources. We know neither the sources (Σ) nor the different weights used to mix the sources (A). To solve this Blind Source Separation (BSS) problem we apply the variational Bayesian Independent Component Analysis (vbICA) algorithm described in Gualandi et al. (2016), consisting in an adaptation of the original Matlab code by Choudrey and Roberts (2003) in order to take into account missing data. The assumptions at the foundation of any ICA technique are: 1) statistical independence of the sources which generated the observations; and 2) linear mix of the sources. The problem consists in finding the right-hand side of the following equation, knowing only the left-hand side:

$$X = A\Sigma + N \tag{1}$$

where A is called the mixing matrix, Σ is the source matrix, and N is zero-mean Gaussian noise. The vbICA solves this problem via a generative model. In practice, the right-hand side unknowns are treated as random variables, and as such they need to be described by a given probability density function (pdf). Since we do not know a priori what the pdf of the sources is, and since we want to model various non-Gaussian signals, the sources are modeled via a Mix of Gaussians (MoG). With a high enough number of Gaussians, a MoG can reproduce any desired pdf. Here we use 4 Gaussians per source, as recommended by Choudrey (2002). To model these Gaussians we need to specify their mean and variance, which are as well treated as random variables. This hierarchical implementation terminates with the definition of hyper-parameters which control the a priori assumptions on the hidden variables that we want to estimate (mixing matrix A, sources Σ, and noise N). The hyper-parameters values are chosen in the attempt to maximize the Negative Free Energy of the model, and are reported in Table S2. The main advantage of the vbICA algorithm over other ICA techniques (e.g., FastICA, Hyvärinen and Oja, 1997) is that it allows more flexibility to recover multimodal probability density functions for the sources.

It is always possible to rescale a given source by a factor α and the corresponding mixing matrix vector by a factor 1/α to obtain the same identical reconstructed matrix. To maintain a similar notation to the more common Singular Value Decomposition, we rewrite equation (1) as:

$$X = USV^T + N \quad (2)$$

where U and V are our spatial distribution and temporal functions, while S is a diagonal matrix. We impose U's and V's columns to be unit norm, as in a regular PCA. The difference with a PCA is that neither U's nor V's columns are constrained to be orthogonal one to the other, i.e. U and V are not orthonormal matrices. Furthermore, the weights in S are not directly related to the amount of the original dataset variance explained, but they still provide an indication of the relative importance of the different ICs in explaining the data. The total variance explained can be directly calculated from the reconstructed time series. For plotting purposes, we then rescale V's columns to be confined between -1 and 1, and we plot in spatial map the corresponding rescaled spatial distribution and weight, which carries the unit of measurement (mm).

Seismic clustering

We briefly describe the clustering algorithm adopted, for which more details can be found in Zaliapin and Ben-Zion (2013). Each event in a seismic catalog can be typically described by 5 parameters: its hypocenter (x, y, z), its time occurrence (t), and its magnitude (m). The distance d between the i-th and j-th events in the catalog is defined as:

$$d_{ij} = \begin{cases} t_{ij}(r_{ij})^{d_f} 10^{-bm_i} & \text{for } t_{ij} > 0 \\ \infty & \text{for } t_{ij} \leq 0 \end{cases} \quad (3)$$

where:

$$t_{ij} = t_j - t_i \quad (4)$$

$$r_{ij} = \sqrt{(x_j - x_i)^2 + (y_j - y_i)^2 + (z_j - z_i)^2} \quad (5)$$

Two parameters are required as input: the fractal dimension d_f of the earthquake hypocenter distribution and the Gutenberg-Richter b value. Here we use $d_f = 1.6$ (default value used in Zaliapin and Ben-Zion, 2013, for Southern California) and b = 0.913 (derived from the Gutenberg-Richter curve on the catalog of Yang et al., 2012). Every earthquake is thus connected to its nearest neighbor in the sense of the distance d. In this way every earthquake is connected to another, and each has a parent event, i.e. an earthquake to which it is directly linked and that preceded it (except for the first event in the catalog). It is also possible to define some rescaled spatial and temporal distances as:

$$T_{ij} = t_{ij} 10^{-0.5bm_i} \quad (6)$$

$$R_{ij} = (r_{ij})^{d_f} 10^{-0.5bm_i} \quad (7)$$

such that d = RT. A threshold d^* is then defined such that earthquakes with $d < d^*$ are considered as strongly linked to the parent event, while if $d \geq d^*$ they are weakly linked (see Results: Comparison with seismicity). In the original work of Zaliapin and Ben-Zion (2013), strongly linked events are named clustered events, while the connection of weakly linked events is discarded and they are named background events.

Results

GPS Independent Components

We extract 12 Independent Components (ICs) from the analysis in the region (Figure 1 and Table S1). The number of ICs is selected using the approach proposed in Gualandi et al. (2016). We consider ICs 1, 5, 6, and 9 (Figures 2 and 3) as potentially tectonic in origin (see Figures S1-S3 and Section S1 of the Supplementary Material for a discussion of the remaining ICs). The largest deformation signal is described by IC1 (Figures 2A and 2B, and S1A and S1B), with post-seismic relaxation still ongoing and including uplift in the Imperial Valley, north of the mainshock. IC6 shows two rapid post-seismic decays, following the EMC mainshock and the M_w 5.7 Ocotillo earthquake (first blue dashed line, Figure 3A). ICs 5 and 9 are more difficult to interpret. The temporal evolution of IC9 (Figures 3C and 3D, and S3A and S3B) shows a very fast decay taking place immediately after the EMC mainshock, lasting about 2 weeks, followed by alternating quiescence and reversals of motion in 2010-11, during the Brawley swarm in 2013, and in 2016-17. These reversals make it implausible that IC9 purely represents fault slip, and they may result from thermal contraction/expansion associated with geothermal production. However, the spatial distribution of IC9 is dominated by the response of stations P506 and P499, which lie next to the Brawley swarm (Figure 3D). These are the same two stations with large displacement associated with IC6 (Figure 3B), and potential cross talk between these two ICs may still be present in our final decomposition. Finally, IC5 (Figures 2C and 2D, and S2A and S2B) shows a large-scale pattern, with far-field displacements larger than the noise level, and with two stations close to the Brawley swarm particularly affected. It is possible that this IC modulates the intensity of the deformation associated with IC1.

Modeling of the tectonic ICs

We first try to model the observed deformation as afterslip (Supplementary Material S2; Figure S4). Deep afterslip can explain the near field horizontal pattern associated with IC1 (Figure S5) but not the near-field vertical observations, and it underpredicts the far-field horizontal deformation. The shorter-term decay IC6 (Figure 3B) is inferred as shallow afterslip at the northern edge of the EMC rupture and in the Yuha Desert, next to the Ocotillo earthquake. The stations on the Mexican side are lacking data in the first months of post-seismic deformation, and we thus discard them for the IC6 modeling. The scarcity of slip on the southernmost segments is likely due to lack of information from the sparse GPS coverage there. The shallow motion is mainly normal, with deeper slip being right-lateral, similar to the results of Gonzalez-Ortega et al. (2014). The normal motion is necessary to explain the subsidence in the Imperial Valley associated with this IC. The addition of IC9 modulates the temporal evolution of the total slip (Figure S6), but the total slip is on average <6% different, and we consider this a secondary signal. IC9 may potentially partially capture poroelastic effects, but these should be concentrated next to the fault [e.g., Gonzalez-Ortega et al., 2014]. The relative contribution of the two earthquakes (EMC and Ocotillo) to the recorded deformation is certainly affected by the asymmetric network coverage, with large importance given to the Ocotillo event due to the high number of stations in its proximity. A better coverage to the Mexican side would have helped resolve these two afterslip processes, but given the available data we can still attempt an estimate of the afterslip relaxation times from the fit of the temporal function V6 with a rate-dependent friction law (green line in Figure 3A, see Section S3 of the Supplementary Material and equation S2). We obtain $\tau_{EMC} = 0.19 \pm 0.10$ yr and $\tau_{Ocotillo} = 0.20 \pm 0.02$ yr.

Although a possible explanation for IC5 is that afterslip is moving in space, and thus more than one IC is needed to keep track of its evolution, its far-field reach and that of IC1 seem more compatible with distributed viscoelastic relaxation. To test this hypothesis, we run a vbICA on the time series of post-EMC viscoelastic relaxation as modeled by Hines and Hetland (2016). We find that their viscoelastic contribution can be described by two ICs whose temporal functions generally resemble those of our ICs 1 and 5, and the first of which also resembles our IC1 in space (Figure 2). This suggests that viscoelastic relaxation is responsible for ICs 1 and 5. However, there are some differences between the two pairs of temporal functions (Figures 2A and 2C). To investigate these, we study the post-seismic temporal evolution generated by a co-seismic rupture of an infinite long strike-slip fault in an elastic plate of thickness H overlying a viscoelastic half-space (see Section S4 of the Supplementary Material). In this case, it is possible to separate spatial and temporal dependencies of surface displacements, which can be written as the result of an infinite sum of spatial and temporal modes [Nur and Mavko, 1974]. We use a combination of the first two modes to fit the two viscoelastic ICs (see equations S10 and S11 in the Supplementary Material), investigating various rheologies (Maxwell, Kelvin-Voigt, Standard Linear Solid, Standard Linear Fluid, and Burgers). Only a bi-viscous material can reproduce the rapid decay in V1's early stage. We find that all rheologies reproduce the slope change in V5 occurring around 2013.0, but only the Burgers rheology reproduces the slope change taking place before 2011 (Figure S7). The long-term behavior of V1 is dictated by the Maxwell-element steady-state viscosity η_1: the higher its values the smaller the curvature of the long-term relaxation. Too high values of η_1 though compromise the ability to fit V5. The best-fitting parameters are μ_1 = 40 GPa, μ_2 = 90 GPa, $\eta_1 = 1.4\times10^{18}$ Pa·s, and $\eta_2 = 2.9\times10^{17}$ Pa·s, where μ_1 and η_1 are the elements of the Maxwell body, and μ_2 and η_2 are those of the Kelvin-Voigt body. The first mode is stronger in the near field but the two modes have more similar magnitudes in the far field, consistent with the character of the spatial terms (Figure S8). This modeling does not aim at substituting more sophisticated analyses which are not the goal of this work (e.g., dynamical forward models, Rollins et al., 2015, or finite element models, Dickinson-Lovell et al., 2018), but it provides a quick way to estimate rheological parameters and it helps convincing ourselves that ICs 1 and 5 are indeed the result of viscoelastic relaxation. Even during the first 8 postseismic months, when IC6 appears to be imaging afterslip, the total surface displacement associated with viscoelastic relaxation (IC1+IC5) is approximately twice as large as that from afterslip.

Comparison with seismicity

The nearest neighbor distances distribution is shown in Figure 4A. Figure 4B shows the same bimodal distribution in a 2-D space with rescaled spatial and temporal distances. Rather than removing the weakly linked events from the spanning tree and classifying them as background seismicity [Zaliapin and Ben-Zion, 2015], we retain them and still consider them as potentially connected to their parent event. Since we do not neglect the potential link with the parent, no matter how weak the link is, we think that the term background seismicity may be misleading. We call strongly and weakly linked events clustered (set C) and non-clustered (set NC), respectively.

All the events connected to a given earthquake belong to its family. For our purposes, we are interested in the EMC and Ocotillo earthquakes' families. We will focus on the immediate offspring, defined by all the events having EMC and Ocotillo earthquakes as parents. The bimodal characteristic separating clustered from non-clustered events is still observable also when considering only the immediate offspring (Figures 4C and 4D). The temporal evolution of the cumulative number of events (magenta line) and the corresponding spatial distribution (squares) are plotted in Figures 3A and 3B for set C, and in Figures 2A and 2B for set NC. The quantities shown in Figures 2, 3, and 4 are reported in the Supplementary Material as Figure S9 and S10 for the Hauksson et al. (2012) seismic catalog. Table S5 summarizes the cumulative number of events and the total moment released depending on the catalog. The differences between the two catalogs likely arise because of the different methods adopted to compile them. While the Hauksson et al. (2012) catalog contains more events and has a considerably larger total moment, Yang et al. (2012) probably has more consistent internal locations being based on a double-difference method.

The cumulative number of immediate offspring events in set C shows a striking match with the afterslip temporal function (Figure 3A). Furthermore, set C events are spatially close to the afterslip (Figure 3B). The moment associated with our best afterslip model, produced from inverting only IC6, is $(8.05\pm0.25)\times10^{18}$ Nm, a factor about one order of magnitude larger than the set C aftershocks, in agreement with Gonzalez-Ortega et al. (2014). This suggests that afterslip was the driving force for these aftershocks [Perfettini and Avouac, 2004]. The link between seismicity and surface geodetic displacement holds also between long-term viscoelastic relaxation and the non-clustered aftershocks (Figure 2A). The viscoelastic relaxation is composed of two contributions, coming from the ICs 1 and 5. We decide to compare the seismicity with the dominant IC1, being aware that discrepancies may arise from the fact that IC5 also contributes to the stress variation induced in the crust. Since weakly linked events have been originally classified as background seismicity [Zaliapin and Ben-Zion, 2013], this finding suggests that time-dependent hazard maps should be considered to improve the hazard estimate after a major earthquake.

From correlation to causation

We further test the effect of each deformation mechanism on sets C and NC by calculating the Coulomb Failure Function variations (ΔCFF). We adopt a friction coefficient of 0.6 and use the clustering results from the catalog of Yang et al. (2012) because it provides also the focal mechanisms, so we can prescribe specific receiver fault parameters for each event. We use the co-seismic slip model from Huang et al. (2017), the afterslip model shown in Figure 3B, and we update the viscoelastic relaxation model from Rollins et al. (2015) via the software Relax (geodynamics.org/cig/software/relax, Barbot et al., 2010a, 2010b) in order to cover the timespan up to the last earthquake in the catalog. This model's grid extends ~300 km outward from the epicenter as a compromise between grid size and good sampling of the coseismic slip given computational limitations, and for self-consistency, we consider only earthquakes within this grid, reducing the number of events in set C from 1135 to 981, and in set NC from 498 to 360. All three mechanisms induced a positive ΔCFF on more than half of the population of events belonging to both sets, as summarized in Table 1. If earthquakes in the two sets are not influenced by a given deformation mechanism, we would expect a 50/50 split between positive and negative ΔCFF. We thus test the null hypothesis for which the probabilities of observing positive and negative values of ΔCFF are equal for a given deformation mechanism and a given set of earthquakes. We can reject the null hypothesis for all mechanisms and both sets at confidence levels larger than 99.99%. In other words, all three deformation mechanisms have positively contributed to the observed seismicity in sets C and NC. From the percentages (see Table 1), afterslip is the dominant mechanism contributing to set C, while viscoelastic relaxation is dominant for set NC.

We then ask if the difference between the percentage of positive ΔCFF induced by one mechanism is significantly larger than the one observed for a competing mechanism. In practice, we use a binomial one-tailed test where the null hypothesis states that the probability $p_+^{mech\,1}$ to have positive ΔCFF from mechanism 1 (e.g., co-seismic slip) is equal to the probability $p_{+}^{mech\,2}$ to have positive ΔCFF from mechanism 2 (e.g., afterslip) for a given set (e.g., set C). For set C, afterslip is the mechanism with the largest percentage of earthquakes with positive ΔCFF, and we can reject the null hypothesis for which the other two mechanisms have the same percentage of positive ΔCFF earthquakes at a confidence level larger than 99.99%. For set NC viscoelastic relaxation is the mechanism with the largest percentage of earthquakes with positive ΔCFF, and we can reject the null hypothesis for which the co-seismic slip has the same percentage of positive ΔCFF earthquakes at a confidence level of 99.47%, while for the comparison with afterslip the confidence level is 82.37%. These results suggest that seismicity is influenced by all three deformation mechanisms, but that afterslip is the leading mechanism which drives clustered aftershocks, while viscoelastic relaxation is the leading mechanism for the non-clustered aftershocks.

Discussion

A common challenge in post-seismic studies is that trade-offs between competing deformation sources make the individual investigation of these mechanisms more difficult. We show that even in a case where data coverage is highly asymmetric, the technique vbICA can not only separate tectonic from non-tectonic sources but can also separate the contributions of afterslip and viscoelastic relaxation. Neither the application of a Principal Component Analysis (PCA, Figures S11-S12) to the studied geodetic time series nor the application of a commonly used ICA technique like FastICA (Figures S13-S14) brings a separation of a short decay from the long one: they are still mixed together with some seasonal signals. Afterslip and viscoelastic relaxation have been invoked to explain post-seismic surface displacements following, for example, the Tohoku-Oki M9.0 [Sun et al., 2014], Bengkulu M8.4 [Tsang et al., 2016], Gorkha M7.9 [Zhao et al., 2017], Izmit M7.4 [Ergintav et al., 2009], and Parkfield M6.0 [Bruhat et al., 2011] earthquakes. For the

Bengkulu earthquake, PCA revealed two major postseismic components [Tsang et al., 2016] with temporal evolutions similar to our viscoelastic ICs (Figures 2A and 2C) but no rapid decay like our IC6 was detected, possibly because the data were not sensitive to near-field afterslip due to the earthquake’s offshore location. For the 2004 Parkfield earthquake, PCA does not separate afterslip and viscoelastic relaxation [Savage and Langbein, 2008] even though both have been invoked [Bruhat et al., 2011]. The potential observation of a small relaxation time would imply the need to reevaluate the friction parameters on the fault: the approach here presented would be helpful for this task, given enough time have passed from the mainshock. Unfortunately we do not have a sufficient coverage in the near-field for the EMC earthquake, but this approach could be tested in better monitored regions like Parkfield.

Seismicity in the proximity (<15 km) of the 2012 Brawley swarm had three crises: one at the end of 2010, the Brawley swarm itself around mid-2012, and one around mid-2016 (Figure 3C, magenta line). All three coincide with periods of enhanced deformation in IC9, suggesting that we have captured the salient deformation in the region. It has been proposed that the Brawley swarm was triggered by aseismic deformation induced by fluid injection [Wei et al., 2015]. Our results point also at triggered deformation in the Brawley region that we have modeled as afterslip on local segments from inversion of IC6. The exclusion of the Brawely segments from the inversion brings similar results for afterslip on the EMC and Ocotillo planes, and simply increases the misfit in the Brawley region. Poroelastic effects may also contribute to the observed deformation, and it has been suggested that aftershocks in the Yuha desert were also driven by fluid migration [Ross et al., 2017]. Fluid pressure variation may affect the count of earthquakes, but the pulse of seismicity associated with fluid migration is, in this case, swarm-like and delayed in time [Ross et al., 2017]. Because of this time delay it is less likely to affect results concerning the immediate offspring, as analyzed here.

We find that, assuming a simple viscoelastic half-space geometry, a bi-viscous material (or a power-law rheology) is needed to explain the early stage of the most relevant viscoelastic IC (Figure 2A). The temporal evolution of the two viscoelastic ICs can be explained by a half-space with Burgers rheology beneath the brittle crust (green line, Figures 2A and 2C). The best rheological parameters are of the same order of magnitude of those found in literature [Pollitz et al., 2012; Gonzalez-Ortega, 2014]. The fact that we need two dashpots (two viscoelastic relaxation times) and one afterslip IC to explain the post-seismic observations is similar to the case of the 1999 Izmit earthquake, where long post-seismic GPS position time series have been fitted using three relaxation times [Ergintav et al., 2009].

Post-seismic deformation is still ongoing more than 7 years after a single M_w 7.2 earthquake, posing challenges for secular rate estimation in geodetic position time series. For a low viscosity region like Southern California, GPS velocities can be perturbed up to 5 mm/yr in the long run [Hearn et al., 2013]. From the modeling of IC1, using the best Burgers viscoelastic parameters we infer that the relaxation is already at more than 90% of its asymptotic value. The remaining 10% will likely sum to ~5 mm in the horizontal direction, and will be below the noise threshold (~1.5 mm) after about 2022.

Viscoelastic relaxation affected the seismicity rate in a region up to several times the fault rupture length and more than 7 years after the mainshock. This offers a potential mechanism to explain long-range earthquake interactions as an alternate to dynamic triggering [Hill et al., 2006]. Observation of delayed triggering at large distances has been reported for the

North Anatolian strike-slip fault after the Izmit earthquake, where aseismic motion in the lower crust/upper mantle was proposed as the cause of stress load in the brittle seismogenic crust [Durand et al., 2010]. The idea that earthquakes can interact at depth through aseismic deformation has been suggested based on seismic observations [Durand et al., 2014; Bouchon et al., 2016; 2018]. Here we have provided a spatio-temporal analysis of both geodetic and seismic data that highlights the connection between seismic and aseismic deformation processes. These findings have implications for our understanding of the "seismic cycle" and for its modeling. In particular, we stress the importance of including viscoelastic relaxation in earthquake-cycle models [Hainzl et al., 1999; Pelletier, 2000; Lambert and Barbot, 2016; Allison et al., 2018], as in this case, for example, we find that it produced larger displacements than afterslip even during the early post-seismic stage.

References

- Allison K.L. and E.M. Dunham (2018), Earthquake cycle simulations with rate-and-state friction and power-law viscoelasticity. Tectonophysics, 733, 232-256, https://doi.org/10.1016/j.tecto.2017.10.021.
- Avouac, J.-P. (2015), From geodetic imaging of seismic and aseismic fault slip to dynamic modeling of the seismic cycle, Annu. Rev. Earth Planet. Sci., 43, 233–71, doi:10.1146/annurev-earth-060614-105302.
- Barbot S. and Y. Fialko (2010a), Fourier-domain Green's function for an elastic semi-infinite solid under gravity, with applications to earthquake and volcano deformation, Geophys. J. Int., 182(2), 568-582, doi: 10.1111/j.1365-246X.2010.04655.x.
- Barbot S. and Y. Fialko (2010b), A unified continuum representation of postseismic relaxation mechanisms: semi-analytic models of afterslip, poroelastic rebound and viscoelastic flow, Geophys. J. Int., 182(3), 1124-1140, doi: 10.1111/j.1365-246X.2010.04678.x.
- Bock Y. et al. (2016) Twenty-Two Years of Combined GPS Products for Geophysical Applications and a Decade of Seismogeodesy. In: Hashimoto M. (eds) International Symposium on Geodesy for Earthquake and Natural Hazards (GENAH). International Association of Geodesy Symposia, vol 145. Springer, Cham
- Bouchon M., D. Marsan, V. Durand, M. Campillo, H. Perfettini, R. Madariaga and B. Gardonio (2016), Potential slab deformation and plunge prior to the Tohoku, Iquique and Maule earthquakes. Nature Geoscience, volume 9, pages 380–383, DOI: 10.1038/NGEO2701.
- Bouchon, M., Marsan, D., Jara, J., Socquet, A., Campillo, M., & Perfettini, H. (2018). Suspected deep interaction and triggering between giant earthquakes in the Chilean

subduction zone. Geophysical Research Letters, 45, 5454–5460. https://doi.org/10.1029/2018GL078350.

- Bruhat L., S. Barbot and J.-P. Avouac (2011), Evidence for postseismic deformation of the lower crust following the 2004 Mw6.0 Parkfield earthquake, JGR, VOL. 116, B08401, doi:10.1029/2010JB008073.
- Bürgmann R. and G. Dresen (2008), Rheology of the Lower Crust and Upper Mantle: Evidence from Rock Mechanics, Geodesy, and Field Observations. Annu. Rev. Earth Planet. Sci. 2008. 36:531–67, DOI: 10.1146/annurev.earth.36.031207.124326.
- Choudrey, R. (2002), Variational Methods for Bayesian Independent Component Analysis, PhD thesis, University of Oxford.
- Choudrey, R. and S. Roberts (2003), Variational mixture of bayesian independent component analyzers, Neural Comput., 15(1), 213–252.
- Durand, V., M. Bouchon, H. Karabulut, D. Marsan, J. Schmittbuhl, M.-P. Bouin, M. Aktar and G. Daniel (2010), Seismic interaction and delayed triggering along the North Anatolian Fault, JGR, VOL. 37, L18310, doi:10.1029/2010GL044688
- Durand, V., M. Bouchon, M. A. Floyd, N. Theodulidis, D. Marsan, H. Karabulut, and J. Schmittbuhl (2014), Observation of the spread of slow deformation in Greece following the breakup of the slab, Geophys. Res. Lett., 41, 7129–7134, doi:10.1002/2014GL061408.
- Ergintav, S., S. McClusky, E. Hearn, R. Reilinger, R. Cakmak, T. Herring, H. Ozener, O. Lenk and E. Tari (2009), Seven years of postseismic deformation following the 1999, M = 7.4 and M = 7.2, Izmit-Düzce, Turkey earthquake sequence. JGR, VOL. 114, B07403, doi:10.1029/2008JB006021.

- Feigl, K.L. and W. Thatcher (2006), Geodetic observations of post-seismic transients in the context of the earthquake deformation cycle, C. R. Geosci., vol. 338, issues 14-15, pp. 1012-1028. https://doi.org/10.1016/j.crte.2006.06.006.
- Freed, A.M. (2007), Afterslip (and only afterslip) following the 2004 Parkfield, California, earthquake, GRL, Vol. 34, L06312, doi:10.1029/2006GL029155.
- Gonzalez-Ortega, A., Y. Fialko, D. Sandwell, F. Alejandro Nava-Pichardo, J. Fletcher, J. Gonzalez-Garcia, B. Lipovsky, M. Floyd, and G. Funning (2014), El Mayor-Cucapah (Mw 7.2) earthquake: Early near-field postseismic deforma- tion from InSAR and GPS observations, J. Geophys. Res. Solid Earth, 119, 1482–1497, doi:10.1002/2013JB010193.
- Gualandi, A., E. Serpelloni, and M. Belardinelli (2016a), Blind source separation problem in GPS time series, J. Geodesy., 90(4), 323–341, doi:10.1007/s00190-015-0875-4.
- Gualandi, A., Perfettini, H., Radiguet, M., Cotte, N., & Kostoglodov, V. (2017b). GPS deformation related to the Mw7. 3, 2014, Papanoa earthquake (Mexico) reveals the aseismic behavior of the Guerrero seismic gap. Geophysical Research Letters, 44(12), 6039–6047.
- Gualandi, A., C. Nichele, E. Serpelloni, L. Chiaraluce, L. Anderlini, D. Latorre, M. E. Belardinelli, and J.-P. Avouac (2017c), Aseismic deformation associated with an earthquake swarm in the northern Apennines (Italy), Geophys. Res. Lett., 44, 7706–7714, doi:10.1002/2017GL073687.
- Hainzl S., G. Zoller and J. Kurths (1999), Similar power laws for foreshock and aftershock sequences in a spring-block model for earthquakes. JGR, VOL. 104, NO. B4, PAGES 7243-7253.

- Hauksson, E., W. Yang and P.M. Shearer (2012), Waveform Relocated Earthquake Catalog for Southern California (1981 to June 2011), Bulletin of the Seismological Society of America, 102 (5): 2239-2244. https://doi.org/10.1785/0120120010.
- Hearn E. H., F. F. Pollitz, W. R. Thatcher, and C. T. Onishi (2013), How do “ghost transients” from past earthquakes affect GPS slip rate estimates on southern California faults?, Geochem. Geophys. Geosyst., 14, 828–838, doi:10.1002/ ggge.20080.
- Hill, D. P., and S. G. Prejean (2006), Dynamic triggering, in Treatise on Geophysics, vol. 4, Earthquake Seismology, edited by G. Schubert and H. Kanamori, chap. 9, pp. 257–291, Elsevier, Amsterdam.
- Hines, T. T., and E. A. Hetland (2016), Rheologic constraints on the upper mantle from 5 years of postseismic deformation following the El Mayor-Cucapah earthquake, J. Geophys. Res. Solid Earth, 121, 6809–6827, doi:10.1002/2016JB013114.
- Huang, M.-H., E. J. Fielding, H. Dickinson, J. Sun, J. A. Gonzalez-Ortega, A. M. Freed, and R. Bürgmann (2017), Fault geometry inversion and slip distribution of the 2010 Mw 7.2 El Mayor-Cucapah earthquake from geodetic data, J. Geophys. Res. Solid Earth, 122, 607–621, doi:10.1002/2016JB012858.
- Hyvärinen, A., and E. Oja (1997), A fast fixed-point algorithm for independent component analysis. Neural. Comput. 9(7):1483–1492. doi:10. 1162/neco.1997.9.7.1483.
- Jónsson, S., P. Segall, R. Pederson and G. Björnsson (2003), Post-earthquake ground movements correlated to pore-pressure transients, Nature, 4242, 179-183.
- Lambert, V., and S. Barbot (2016), Contribution of viscoelastic flow in earthquake cycles within the lithosphere-asthenosphere system, Geophys. Res. Lett., 43, 10,142–10,154, doi:10.1002/2016GL070345.

- Liu, Z., S. Owen, D. Dong, P. Lundgren, F. Webb, E. Hetland and M. Simons (2010a), Estimation of interplate coupling in the Nankai trough, Japan using GPS data from 1996 to 2006, Geophys. J. Int., 181, 1313-1328, doi: 10.1111/j.1365-246X.2010.04600.x.
- Luen B. and P.B. Stark (2012), Poisson tests of declustered catalogs, Geophys. J. Int., doi:10.1111/j.1365-246X.2012.05400.X.
- Nur A. and G. Mavko (1974), Postseismic Viscoelastic Rebound. Science **183** (4121), 204-206. DOI: 10.1126/science.183.4121.204.
- Pelletier J.D. (2000), Spring-block models of seismicity: Review and analysis of a structurally heterogeneous model coupled to a viscous asthenosphere, in GeoComplexity and the Physics of Earthquakes, Geophysical Monograph Series number 120, Editors: J.B. Rundle, D.L. Turcotte and W. Klein.
- Perfettini, H., and J.-P. Avouac (2004), Postseismic relaxation driven by brittle creep: A possible mechanism to reconcile geodetic measurements and the decay rate of aftershocks, application to the Chi-Chi earthquake, J. Geophys. Res., 109, B02304, doi:10.1029/2003JB002488.
- Perfettini, H. and J.-P. Avouac (2007), Modeling afterslip and aftershocks following the 1992 Landers earthquake, JGR Solid Earth, 112, B7, https://doi.org/10.1029/2006JB004399.
- Pollitz F.F, R. Burgmann and W. Thatcher (2012), Illumination of rheological mantle heterogeneity by the M7.2 2010 El Mayor-Cucapah earthquake, G3, Volume 13, Number 6, doi:10.1029/2012GC004139.
- Reasenberg P. (1985), Second-order moment of central California seismicity, 1969-82, J. Geophys. Res., 90, 5479-5495.
- Rollins C., S. Barbot and J.-P. Avouac (2015), Postseismic Deformation Following the 2010 M 1⁄4 7:2 El Mayor-Cucapah Earthquake: Observations, Kinematic Inversions,

and Dynamic Models, Pure Appl. Geophys. 172, 1305–1358, DOI 10.1007/s00024-014-1005-6.

- Ross, Z.E., C. Rollins, E.S. Cochran, E. Hauksson, J.-P, Avouac and Y. Ben-Zion (2017), Aftershocks driven by afterslip and fluid pressure sweeping through a fault-fracture mesh, Geophys. Res. Lett., 44, 8260-8267, doi:10.1002/2017GL074634.
- Savage, J. (1990), Equivalent Strike-Slip Earthquake Cycles in Half-Space and Lithosphere-Asthenosphere Earth Models, JGR, VOL. 95, NO. B4, PAGES 4873-4879.
- Savage J.C. and J. Langbein (2008), Postearthquake relaxation after the 2004 M6 Parkfield, California, earthquake and rate-and-state friction. J. Geophys. Res., 113, B10407, doi:10.1029/2008JB005723.
- Serpelloni, E., Pintori, F., Gualandi, A., Scoccimarro, E., Cavaliere, A., Anderlini, L., et al. (2018). Hydrologically induced karst deformation: Insights from GPS measurements in the Adria-Eurasia plate boundary zone. Journal of Geophysical Research: Solid Earth, 123, 4413–4430. https://doi.org/10.1002/2017JB015252.
- Suito, H. and J.T. Freymueller (2009), A viscoelastic and afterslip postseismic deformation model for the 1964 Alaska earthquake, JGR, 114, B11404, doi:10.1029/2008JB005954.
- Sun T., K. Wang, T. Iinuma, R. Hino, J. He, H. Fujimoto, M. Kido, Y. Osada, S. Miura, Y. Ohta and Y. Hu (2014), Prevalence of viscoelastic relaxation after the 2011 Tohoku-oki earthquake, Nature, Vol. 514, 84-87, doi:10.1038/nature13778.
- Tsang, L. L. H., E. M. Hill, S. Barbot, Q. Qiu, L. Feng, I. Hermawan, P. Banerjee, and D. H. Natawidjaja (2016), Afterslip following the 2007 Mw 8.4 Bengkulu earthquake in Sumatra loaded the 2010 Mw 7.8 Mentawai tsunami earthquake rupture zone, J. Geophys. Res. Solid Earth, 121, 9034–9049, doi:10.1002/2016JB013432.

- Wei S., J.-P. Avouac, K.W. Hudnut, A. Donnellan, J.W. Parker, R.W. Graves, D. Helmberger, E. Fielding, Z. Liu, F. Cappa and M. Eneva (2015), The 2012 Brawley swarm triggered by injection-induced aseismic slip, EPSL, 422, 115-125, http://dx.doi.org/10.1016/j.epsl.2015.03.054.
- Yang, W., E. Hauksson and P.M. Shearer (2012), Computing a Large Refined Catalog of Focal Mechanisms for Southern California (1981–2010): Temporal Stability of the Style of Faulting, Bulletin of the Seismological Society of America, 102 (3): 1179-1194. https://doi.org/10.1785/0120110311.
- Zaliapin I. and Y. Ben-Zion (2013), Earthquake clusters in southern California I: Identification and stability, JGR: Solid Earth, VOL. 118, 2847–2864, doi:10.1002/jgrb.50179.
- Zhao, B., Bürgmann, R., Wang, D., Tan, K., Du, R., & Zhang, R. (2017). Dominant controls of downdip afterslip and viscous relaxation on the postseismic displacements following the Mw 7.9 Gorkha, Nepal, earthquake. Journal of Geophysical Research: Solid Earth, 122, 8376–8401. https://doi.org/10.1002/2017JB014366.

Acknowledgments

The GPS position time series are available at: ftp://sopac-ftp.ucsd.edu/pub/timeseries/measures/ats/WesternNorthAmerica/previous/, file WNAM_Clean_DetrendNeuTimeSeries_jpl_20171216.tar. The seismic catalogs are available at: http://scedc.caltech.edu/research-tools/alt-2011-dd-hauksson-yang-shearer.html and http://scedc.caltech.edu/research-tools/alt-2011-yang-hauksson-shearer.html. The vbICAIM code is available from the corresponding author on reasonable request. We thank Ilya Zaliapin, Yehuda Ben-Zion, and Zachary Ross for providing the seismic clustering code and valuable feedback. We thank Jean-Philippe Avouac for useful discussions and Trever Hines for sharing the modeled position time series to compare with our analysis. We thank Roland Bürgmann for valuable comments who helped improving the manuscript.

Figures

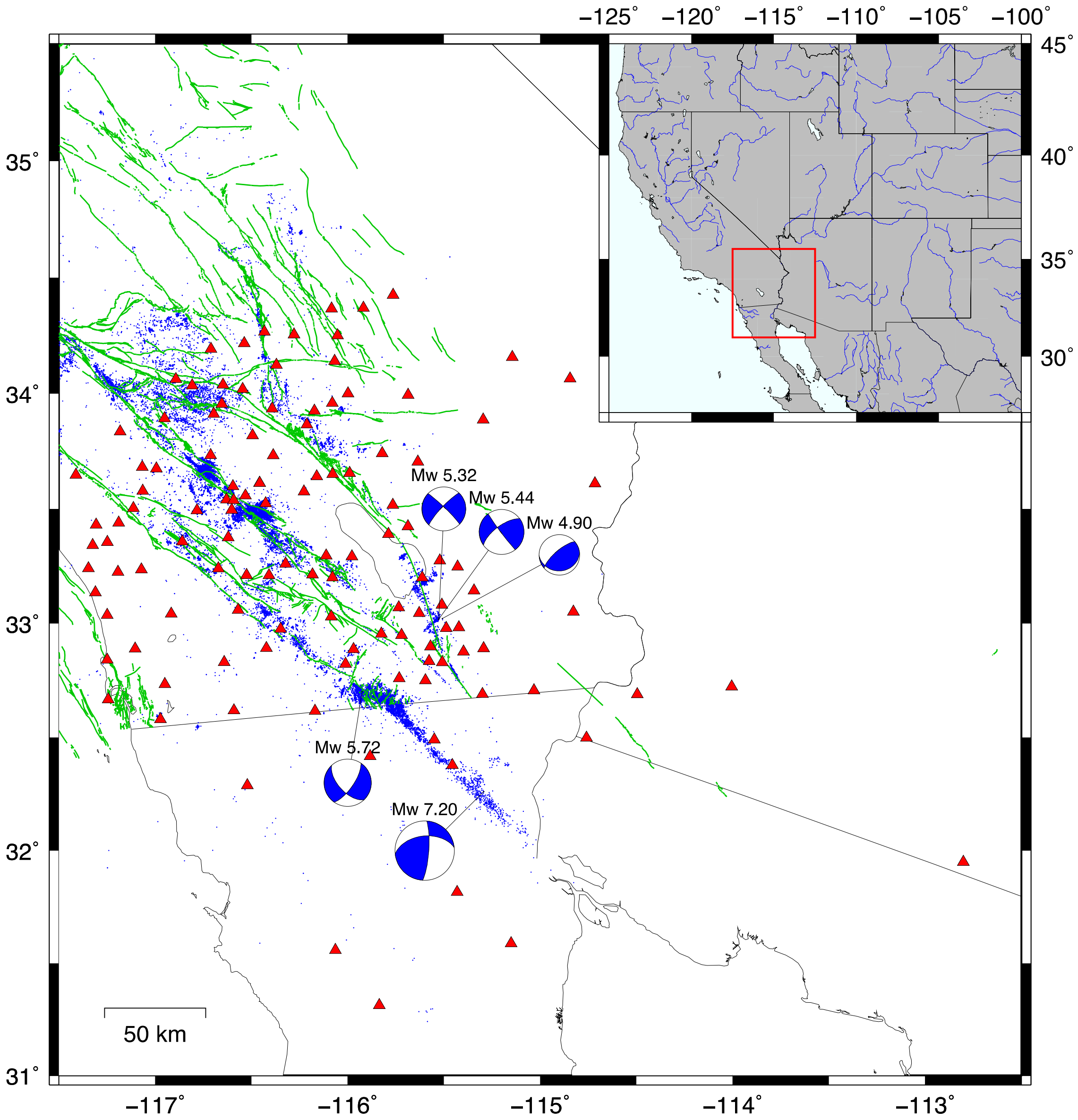

Figure 1: **Study region.** Red triangles: Continuous GPS stations. Blue dots: Seismicity after the El Mayor-Cucapah earthquake from ref. 9, updated to 2017/09/30 (M_c = 2.0). Beach balls: Focal mechanisms of El Mayor-Cucapah (Mw 7.2), Ocotillo earthquake (Mw 5.72), and Brawley swarm major events (Mw 5.32, 5.44, and 4.90). Green lines: Surface fault traces from USGS catalog (https://earthquake.usgs.gov/hazards/qfaults/). Insert map: West United States and Mexico. Red square: region of interest.

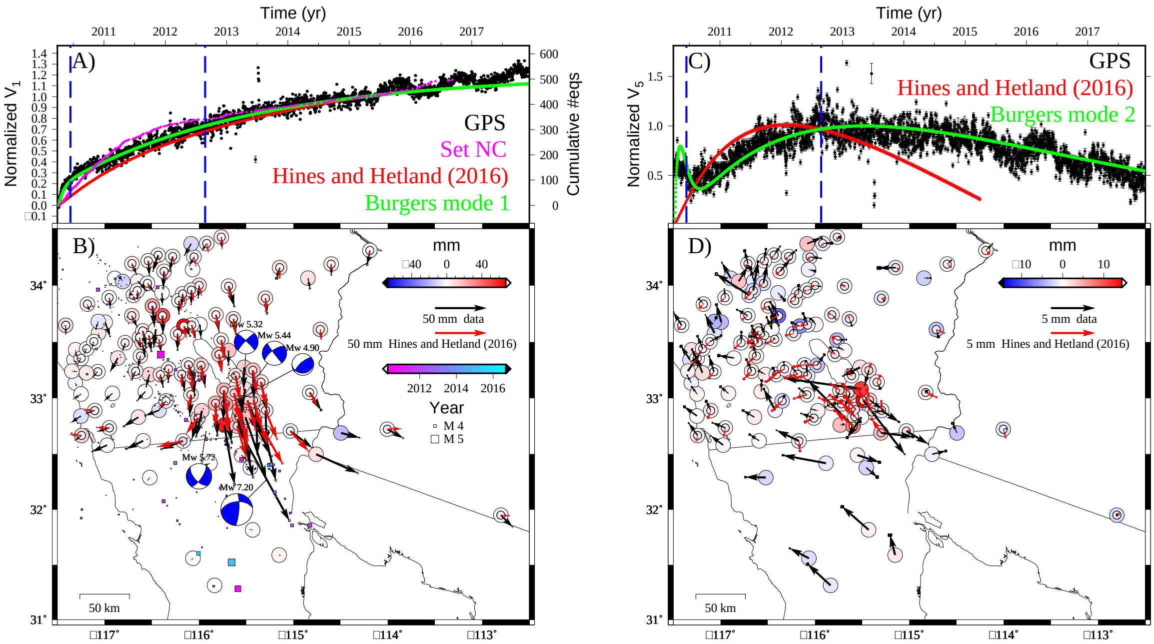

Figure 2: **Spatio-temporal viscoelastic post-seismic deformation.** (A) Black: GPS IC1 temporal evolution and corresponding standard deviation. Red: viscoelastic IC1 temporal evolution of ref. 16 model. Green: Burgers pure mode 1 temporal evolution for $\mu_{Maxwell} = 40\ GPa$, $\eta_{Maxwell} = 1.4 \times 10^{18} Pa \cdot s$, $\mu_{Kelvin-Voigt} = 90\ GPa$,, $\eta_{Kelvin-Voigt} = 2.9 \times 10^{17} Pa \cdot s$. Magenta: Cumulative number of earthquakes weakly linked (non-clustered, set NC) to EMC and Ocotillo earthquakes. Blue vertical lines: Ocotillo earthquake and Brawley swarm epochs. (B) Map view of the corresponding spatial distributions. Arrows/Circles: horizontal/vertical spatial distribution. Black arrows and outer circles are for GPS derived analysis. Red arrows and inner circles are for the analysis on ref. 16 model. For some stations no model is available (no inner circle and no red arrow displayed). Squares: earthquakes set NC spatial distribution. (C) and (D) as (A) and (B) but for IC5, with Burgers pure mode 2.

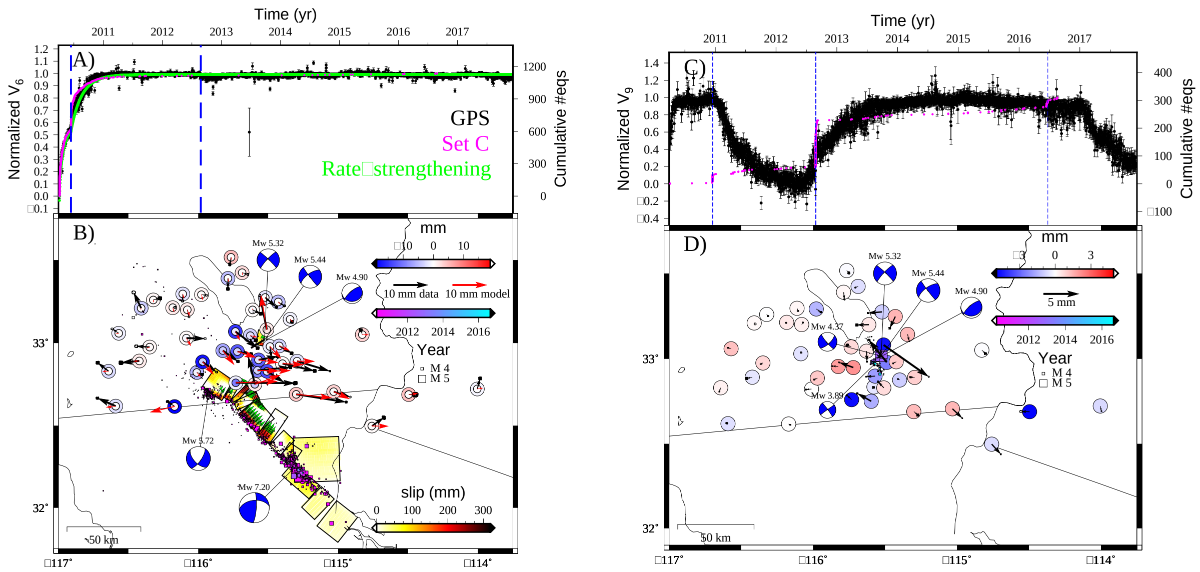

Figure 3: **Spatio-temporal afterslip and Brawley swarm deformation.** (A) Black: GPS IC6 temporal evolution and corresponding standard deviation. Green: Best fit with a rate-strengthening afterslip function (equation S3). Magenta: Cumulative number of earthquakes strongly linked (clustered, set C) to EMC and Ocotillo earthquakes. Blue vertical lines: Ocotillo earthquake and Brawley swarm epochs. (B) Map view of the corresponding spatial distributions. Arrows/Circles: horizontal/vertical spatial distribution. Black arrows/Outer circles: data derived. Red arrows/inner circles: modeled. Squares: earthquakes set C spatial distribution. (C) as (A) but for IC9 (black), and cumulative number of events in a 15 km radius from the largest Brawley swarm event (Mw 5.41, -115.5403E, 33.0185N). Blue dashed lines mark epochs when events with Mw>4.0 occurred.

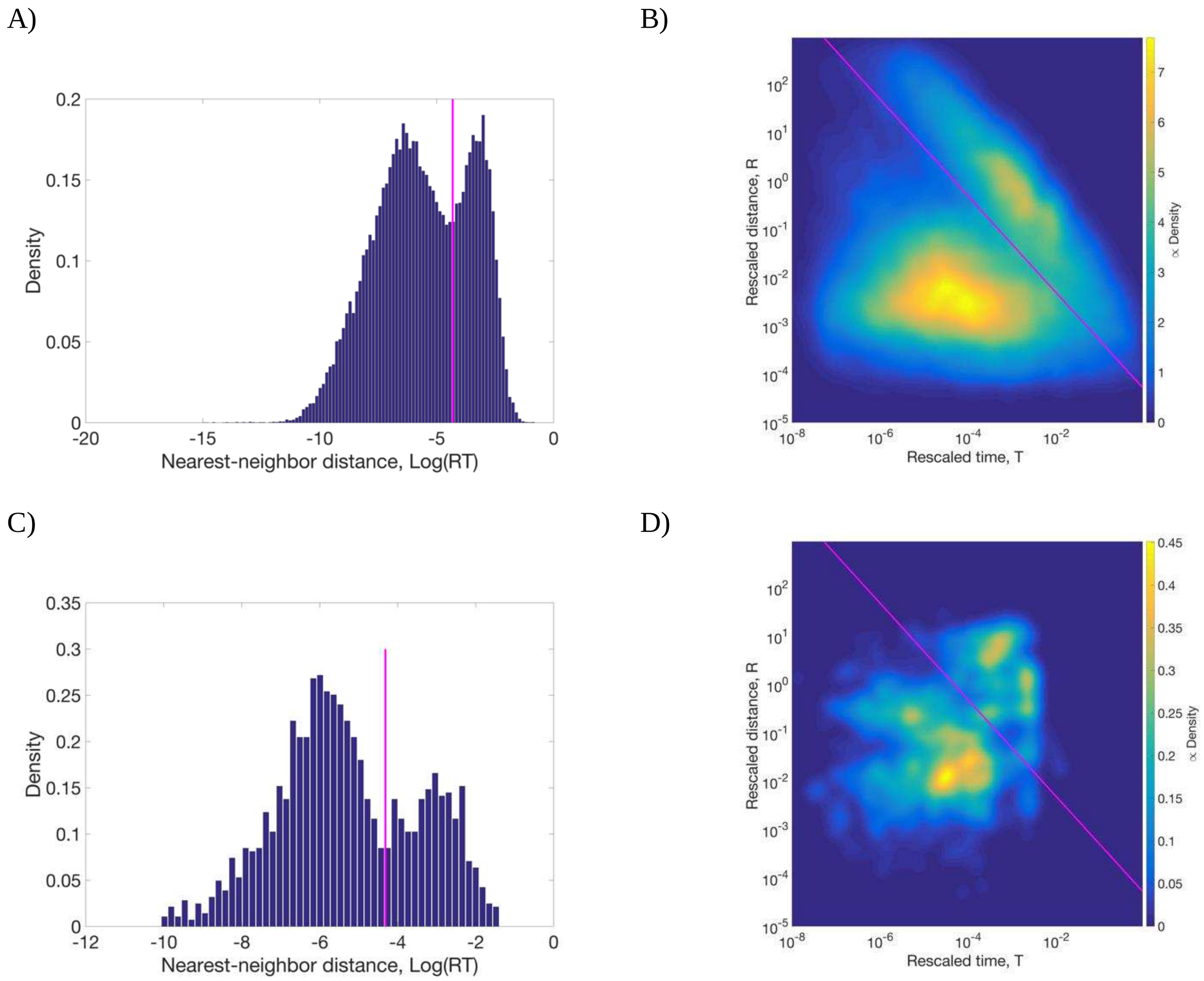

Figure 4: **Seismic nearest neighbor distribution.** Left: Histogram of the nearest-neighbor distance d = RT. Right: Joint distribution of rescaled time T and space R, rescaled by $10^{-0.5bm}$, with b = 0.913 from the Gutenberg-Richter relation and M being the magnitude of the parent event. Top: Entire catalog from ref. 9, containing seismicity from 1981 and updated to 30/09/2016. Bottom: Immediate offspring of EMC and Ocotillo earthquakes. Magenta line in all panels: Threshold $d^* = 10^{-4.3154}$.

	% of earthquakes such that $\Delta CFF > 0$	
	Set C	**Set NC**
Co-seismic slip	**61.32%**	**63.86%**
Afterslip	**71.10%**	**64.66%**
Viscoelastic relaxation	**62.57%**	**72.56%**

Table 1: Percentage of earthquakes with positive ΔCFF for different deformation mechanisms. The total number of earthquakes in set C is 1135, and in set NC is 498. For the viscoelastic calculations the number of earthquakes in set C is 981, and in set NC is 360.